Blumenthal et al. *EPJ Quantum Technology* (2023) 10:46
https://doi.org/10.1140/epjqt/s40507-023-00203-z

EPJ Quantum Technology
a SpringerOpen Journal

RESEARCH Open Access

# Multiple electron pumping

Mark D. Blumenthal[1*], Declan Mahony[1], Salahuddeen Ahmad[1], Dominique Gouveia[1], Hume Howe[2], Harvey E. Beere[3], Thomas Mitchel[3], Dave A. Ritchie[3] and Michael Pepper[2]

*Correspondence:
mark.blumenthal@uct.ac.za
[1]Department of Physics, University of Cape Town, Rondebosch, Cape Town, 7700, South Africa
Full list of author information is available at the end of the article

**Abstract**

The need to pump single electrons with a high degree of accuracy and fidelity has led to the development of a range of different pump and turnstile designs. Previous pumping mechanisms have all demonstrated that pumping more than one electron per cycle degrades the quantisation of the measured current. This unreliable delivery of multiple electrons per cycle has limited the use of on-demand single electron sources in electron quantum optic experiments. We present highly quantised current with multiple electrons pumped per cycle. We experimentally demonstrate that in our pumps an increase in electron throughput per cycle does not lead to an appreciable degradation in the accuracy of the produced current.

Our pump is realised in an aluminium gallium arsenide two-dimensional electron gas, where electrons are pumped through a one-dimensional split-gate confinement potential under the influence of an applied source-drain voltage $V_{SD}$, and where the pump is driven by a trapezoidal arbitrary waveform. This combination of a split-gate potential, $V_{SD}$ bias and trapezoidal wave form has led to the observation of robust quantised plateaus where not just a single electron, but a multiple integer number of electrons are pumped per cycle with a high degree of robustness and without the need of a magnetic field. For seven electrons per cycle, we report an increase of over two orders of magnitude in pumping accuracy from $2.72 \times 10^{-2}$ in devices operating in the conventional pumping regime, to $1.64 \times 10^{-4}$ in pumps operating in what we call the long plateau regime, a regime accessed under a change in a split-gate pumps applied $V_{SD}$ voltage. This pump will find direct use in quantum transport measurements where the metrological accuracy of single electrons pumped per cycle is not required and the low throughput per cycle of electrons is limiting.

**Keywords:** Quantum information; Quantum entanglement; Single-electron; Quantum dot; Electron pump; Electron quantum optics

## 1 Introduction

There is considerable interest in pumping multiple electrons per cycle in the field of solid-state quantum information processing [1]. This includes work on flying qubits [2, 3], electron interferometry [4], and electron pair partitioning [5–12]. Traditionally, experiments performed on quantized acousto-electric effect devices [13–15] and finger gate pumps [16–18] are limited to pumping just one or two electrons per cycle, as an increase in the number of electrons per cycle degrades the quantisation of the pumped current plateaus [19]. Current quantisation can be improved with the application of a high perpen-

dicular magnetic field [20–22] or driving the pump with a custom trapezoidal waveform instead of a sinusoidal [23]. In the Experimental Results section we present our findings when applying a customised trapezoidal RF waveform to a recently published [24] new pump design where the quantum dot is defined using a split-gate, finger-gate pair and the pump is operated in what we define as the long pumping regime (LPR). By combining the split-gate QD geometry with a trapezoidal RF waveform for the first time, we demonstrate the ability to pump multiple electrons (greater than three) per cycle with an accuracy and robustness not before seen in any other single electron pump and without the need of a magnetic field.

In the Discussion section we attempt to explain this new pumping regime by investigating the screened potential, gate energies, source drain bias, single particle energy states as well as RF signal where we explicitly look at the trapezoidal waveform and discuss the effects it has on the pumping mechanism.

## 2 Experimental results

### 2.1 Device and experimental setup

The device design and experimental setup is given in Fig. 1a). A Ti/Au entrance finger gate (red) and split gate (green) are used to define the entrance and exit gate respectively of the QD in the AlGaAs 2DEG. DC voltages were applied to all gates using a NI2969 cDAQ with the RF signal coupled to the exit gate via a bias tee. The RF source used was a HP E4400B for driving a simple sinusoidal wave. When driving the pump with a trapezoidal wave form a AWG7122C Tektronix model arbitrary waveform generator was used.

The device was fabricated on MBE grown high mobility GaAs/$Al_xGa_{1-x}As$ Si-doped 2DEG wafers with the 2DEG 90 nm below the surface (10 nm GaAs cap, 40 nm Si-doped GaAs/$Al_xGa_{1-x}As$, 40 nm GaAs/$Al_xGa_{1-x}As$ spacer, and GaAs substrate with a carrier density $n = 1.9 \times 10^{11}$ cm$^{-2}$ and mobility $\mu = 1.014 \times 10^6$ cm$^2$/Vs). The 2DEG channel pattern was defined using electron-beam lithography (EBL) and etched to a depth of 40 nm using wet chemistry. The gates were defined using EBL and deposited with Ti/Au in a thermal evaporator. The split gate has a width and gap of 400 nm, whilst the finger gate a width of 150 nm. The pitch of the gates are 200 nm. The sample was loaded into a Leiden Cryogenics dilution fridge with a base temperature of 7 mk. The pumped current was measured using a Keithley 6430 source measure unit (SMU), which was connected to the drain side of the pump. The source side was grounded.

### 2.2 Pumpmaps

Pumping in the conventional pumping regime (CPR) or LPR is determined by the magnitude of the applied source-drain bias $V_{SD}$ in such split-gate, finger-gate pumps [24]. The exact dimensions of the split-gate also has an impact. A systematic study of the effects of the split-gate geometry remains the subject of further investigations. In Fig. 1b) the CPR is shown with the $V_{SD}$ bias set to 0 mV and a RF sinusoidal wave applied to the entrance finger-gate $V_{ent}$. This pump map was taken from a different device utilising the same finger-gate split-gate geometry, but with slightly different dimensions. The first seven plateaus are indicated on the plot. As the number of pumped electrons increases, plateaus become narrower in $V_{exit}$ and degrade due to an increase in slope [25]. This is an indication of the break down in pump accuracy for multiple integer pumping as reported in previous studies [26, 27], where electron-electron interactions suppress the plateau length and accuracy. In such split-gate finger gate pumps an increase in source drain bias (for-

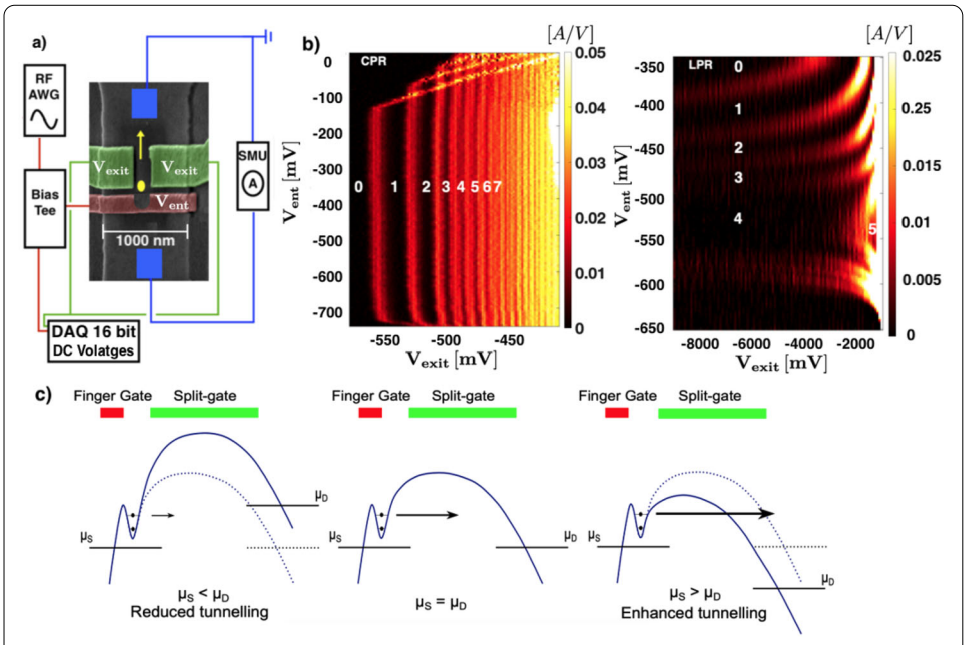


**Figure 1** a) Electron microscope image of the device used in the LPR and schematic of the experimental setup. RF and DC voltage are applied to the finger-gate (red) and only DC voltage is applied to the split-gate (green). b) Numerical derivative pump maps in the CPR ($f$ = 180 MHz with amplitude Amp = 1 $V_{pp}$) and LPR (fundamental $f$ = 181.81 MHz with Amp = 1 $V_{pp}$) of the pumped current with a tailored trapezoidal signal from the AWG applied in the LPR. c) Schematic showing the same snap shot during the pump cycle for different $V_{SD}$ bias $V_{SD}$ regimes. The dotted lines in the left and right schematic correspond to the form of the exit barrier in the middle schematic where $V_{SD} = 0$ and is used as a comparative reference point

ward biased) tunes the pump into the LPR regime as demonstrated in Hume *et al.* [24], but now we also apply a trapezoidal signal to $V_{ent}$ instead of a standard sinusoidal wave. This produces a pump map in the LPR regime given in Fig. 1b). This novel pump map now dramatically modified in structure, differing not only from the form when operating in the CPR but now with the application of a trapezoidal signal, also from what was reported by Howe *et al.* [24]. The LPR pump map, shows the first four plateaus clearly visible with the fifth starting to emerge from the right. In comparison to the pumpmap produced in the CPR, all plateaus are well defined and remain equally robust in $V_{exit}$, with an increase in robustness in $V_{ent}$ with the fourth plateau. The number of electrons that are pumped per cycle for a fixed $V_{ent}$ and $V_{exit}$ can be precisely controlled with the applied $V_{SD}$ voltage, see Fig. 2c) and corresponding discussion that follows.

In Fig. 1c), schematics showing a snap shot in time during the pump cycle for different applied source drain voltages $V_{SD}$ represented by the chemical potential energy of the leads($\mu_s, \mu_d$) are given. What follows is a qualitative description of the pumping mechanism and the effects the applied $V_{SD}$ voltages have on the exit split-gate potential energy. A rigorous quantitative investigation incorporating not just the effects of the $V_{SD}$ voltage, but also gate geometry as well as the explicit wave form of the RF signal is presented in the Discussion section later on in the paper.

In all three schematics in Fig. 1c), the gates defining the potential profile are indicated by the colour bars with the finger-gate (red) on the left and the split-gate (green) on the right. The broadness of the potential on the right is due to the larger dimensions of the split-gate versus the finger-gate. The RF signal is only applied to the finger-gate on the left. In all

three schematics, the QD energy profile has been taken at a time in the pump cycle when the entrance gate potential energy has risen up through the Fermi level in the source ($\mu_s$) forming a QD with two electrons captured. The DC voltages, RF frequency and amplitude are the same in all schematics. Only the applied $V_{\mathrm{SD}}$ voltage differs between schematics as shown. The pumping mechanism requires that as time progresses the entrance gate potential energy rises further up as the gate becomes more negative due to the RF signal, bringing the trapped electrons in the dot closer to the point where they can leave via the exit gate. If the energy of the occupied electron states within the dot are at least aligned with the exit barrier energy, electrons will leave the dot via the drain. Here with the split-gate exit barrier as apposed to conventional pumps with a finger-gate exit barrier, the $V_{\mathrm{SD}}$ bias can be used as a tuning parameter impacting the likelihood for the electrons to leave the dot via the exit split-gate. The centre schematic shows the time snap with $\mu_s = \mu_d$. The two captured electrons for the set parameters (DC gate voltages, RF power and frequency) remain trapped with a close to zero probability of leaving the dot to the drain. For this discussion we take the centre schematic as the reference state. Without altering the set parameters, in the left schematic only the $V_{\mathrm{SD}}$ voltage is changed such that $\mu_s < \mu_d$. This causes a marked increase in the potential energy of the exit gates (the dotted line shows the potential energy of the exit gate when $\mu_s = \mu_d$) resulting in stronger confinement of the electrons decreasing further the likelihood the electrons will leave to the drain. In the right schematic, once again the set parameters are left unchanged but now the the $V_{\mathrm{SD}}$ voltage is changed such that $\mu_s > \mu_d$. Here the exit gate potential energy is reduced substantially bringing the captured electron states in resonance with the exit barrier allowing for the electrons to leave via the drain as pumped quantised current.

### 2.3 RF wave form and $V_{\mathrm{SD}}$ dependence

In Fig. 2a), single line scans of the normalised pumped current operating in the conventional pumping regime (CPR) (blue) and the LPR (red) are shown. For the LPR an RF trapezoidal waveform (inset Fig. 1a) red) is applied with a pulse width fixed at 0.5 ns and rise time 4.0 ns. The slope on the falling edge of the trapezoidal pulse is a sinusoidal segment with frequency 62.5 MHz. The pulses shown in the inset have been converted from gate voltage to the potential energy on the gate. The voltage signal from the AWG has an amplitude of 1 $V_{\mathrm{pp}}$, sampled at 12 GS/s, with 66 sample points per cycle, to give a frequency of 181.81 MHz. In the case of the CPR, a simple sinusoidal signal (inset Fig. 1a) blue) with $f$ = 180.0 MHz and amplitude of 1 $V_{\mathrm{pp}}$ is applied. In both cases $V_{\mathrm{ent}} = -425$ mV. Noticeable is the scale of $V_{\mathrm{exit}}$ on the x-axis, contrasting the enhanced robustness in the plateau length when operating in the LPR instead of the CPR, with over an order of magnitude difference. Analysis on the effects the different wave forms have on the entrance gate potential is presented in the Discussion section. As detailed in Giblin *et al.* [23] the use of a trapezoidal signal allows for a tailored signal to be constructed such that at critical stages in the pump cycle such as the loading of electrons into the QD from the source, the oscillating entrance gate is slowed. At stages less critical such as the ejection of electrons to the drain and subsequent return to the start of loading the dot again, the signal is sped up. In such a way, the overall duty cycle of the pump is preserved to ensure high throughput of current.

In Fig. 2b) a pump map shows the formation of high integer single electron plateaus (two to seven) in the LPR with the same trapezoidal RF signal for different $V_{\mathrm{SD}}$ voltages. $V_{\mathrm{ent}}$ is fixed to −530 mV. $V_{\mathrm{exit}}$ is swept from −9000 mV to −1000 mV on the x-axis, whilst

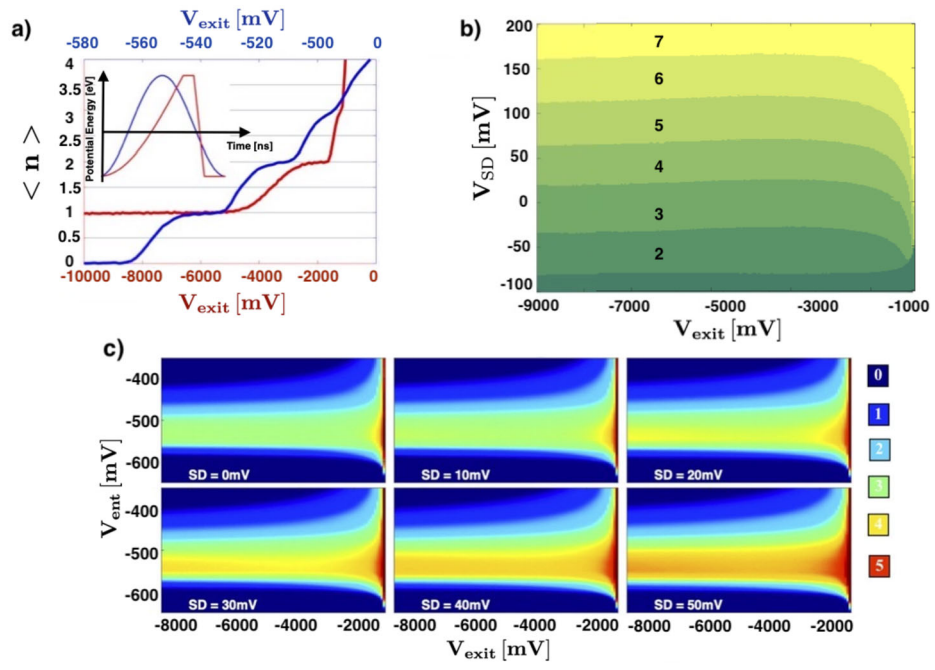


**Figure 2** a) Single line scans of the normalised pumped current operating in the LPR (red) and the (CPR) (blue). $V_{ent}$ = –425 mV for both scans. Inset: Tailored trapezoidal signal from the AWG(red) and sinusoidal RF signal(blue). The signals have been converted from voltage to potential energy b) Pump map of $V_{SD}$ voltage versus $V_{Exit}$ of the normalised pumped current in the LPR. $V_{ent}$ = –530 mV. c) Pumpmaps of $V_{ent}$ versus $V_{exit}$ in the LPR showing the transition to higher pumped integer current as the $V_{SD}$ voltage is increased in 10 mV steps. The change from a monochromatic RF sinusoidal signal to a synthesised trapezoidal signal, leads to dramatically different pumpmaps when compared to the CPR (Fig. 1b). In the LPR pump maps in b) and c). $f$ = 181.81 MHz with Amp = 1 $V_{pp}$

the $V_{SD}$ bias is stepped from –100 mV to 200 mV in 1 mV steps on the y-axis. On simple inspection there is no gradual shortening of the length of the plateaus in $V_{exit}$ with an increase in electron number per cycle as is the case in the CPR. An increase in robustness with $V_{exit}$ is observed in the form of the pump map however the same stability in $V_{SD}$ is not apparent. In metrology, the level of accuracy of a pump operating in the CPR is usually presented in-terms of the $V_{exit}$ [28] only. Here we present our results utilising the same convention.

In Fig. 2c) a series of pump maps from the split-gate finger-gate pump operating in the LPR with a trapezoidal RF signal applied, shows the progression of the maps as the $V_{SD}$ bias is changed from 0 mV to 50 mV in steps of 10 mV. The colour key on the bottom left corner of the figure indicate the number of electrons pumped per cycle for different $V_{ent}$ and $V_{exit}$ of the pumpmap. Striking is the evolution of the plateaus to a higher integer number of pumped electrons as the $V_{SD}$ voltage is changed, for the same set of DC gate voltages and without any discernible change in the structure of the pump map. As the $V_{SD}$ voltage is increased the fourth and fifth plateau (indicated in yellow and red respectively) emerge monotonically from right to left. The evolution of the plateaus to higher integer number of pumped current in such a manner has not been observed before and is only observed when a trapezoidal RF signal is utilised.

A more in-depth analysis of these effects is presented in the Discussion section of the paper.

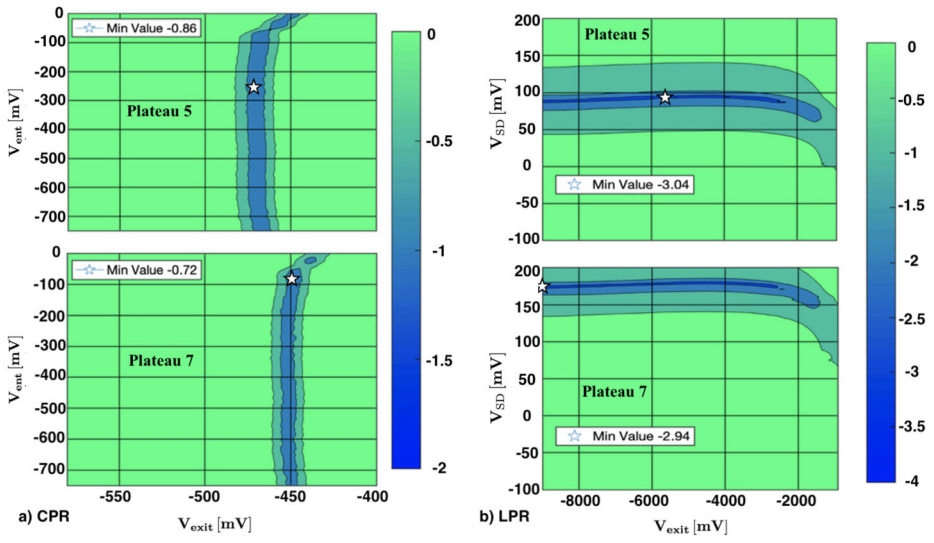


**Figure 3** a) Pumpmaps of $V_{ent}$ versus $V_{exit}$ in the CPR for plateaus five and seven. $\log_{10}|n - \frac{I}{ef}|$ is represented by the colourbar. b) Pumpmaps of $V_{SD}$ Voltage versus $V_{exit}$ in the LPR for plateaus five and seven. $\log_{10}|n - \frac{I}{ef}|$ is represented by the colourbar. The white stars indicate the [x,y] position of the minimum value of $\log_{10}|n - \frac{I}{ef}|$, with the numerical value quoted in the white boxes. In the CPR, $f$ = 180 MHz with amplitude Amp = 1 $V_{pp}$ and $V_{SD}$ = 0 mV. In LPR the fundamental is $f$ = 181.81 MHz with Amp = 1 $V_{pp}$ and $V_{ent}$ = –530 mV

## 2.4 Pump accuracy

Quantitative analysis based on work by Giblin *et al.* [28] was carried out to determine how the accuracy of the pumped current in the LPR and CPR changes when the number of electrons transported per cycle is increased.

Figure 3 shows the $\log_{10}|n - \frac{I}{ef}|$ for both the CPR and LPR presented as a set of pumpmaps, where $n$ an integer, represents the number of pumped electrons expected on the plateau under investigation, $I$, the measured pumped current, $f$, the first harmonic of the synthesised trapezoidal RF signal in the LPR or the only harmonic in the case of the sinusoidal RF signal in the CPR and $e$ the charge of the electron. High integer plateaus for $n$ = 5 and $n$ = 7 are shown. For the CPR, Fig. 3a), the plateaus are shown in $V_{exit}$ with $V_{ent}$ stepped on the y-axis, the $V_{SD}$ bias is set to 0 mV. For the LPR, the plateaus are shown in $V_{exit}$ with the $V_{SD}$ voltage stepped on the y-axis. $V_{ent}$ = –530 mV. The white stars indicate the minimum value of $\log_{10}|n - \frac{I}{ef}|$ with the numerical value of this minimum quoted in the white boxes. The smaller the minimum value, the closer the normalised pumped current is to the expected integer value $n$. The corresponding [x,y] settings in the case of the CPR [$V_{ent}$,$V_{exit}$] and for the LPR [$V_{SD}$,$V_{exit}$] give the respective parameter voltages where the value of pumped current differs the least from the expected value given by $I = nef$. A moving average of ten data points applied in the direction of $V_{exit}$ was taken to smooth the produced pumpmaps. In comparing Fig. 3a) to Fig. 3b), the minimum value $\text{Min}(\log_{10}|n - \frac{I}{ef}|)$ obtained for the plateaus $n$ = 5 and $n$ = 7 in the LPR is considerably smaller than that in the CPR. This was the case for all plateaus from $n$ = 1 to $n$ = 7. The colour bar range representing $\text{Min}(\log_{10}|n - \frac{I}{ef}|)$ in Fig. 3 indicates a remarkable improvement in accuracy and robustness for the LPR in $V_{exit}$ when compared to the CPR with over two orders of magnitude improvement.

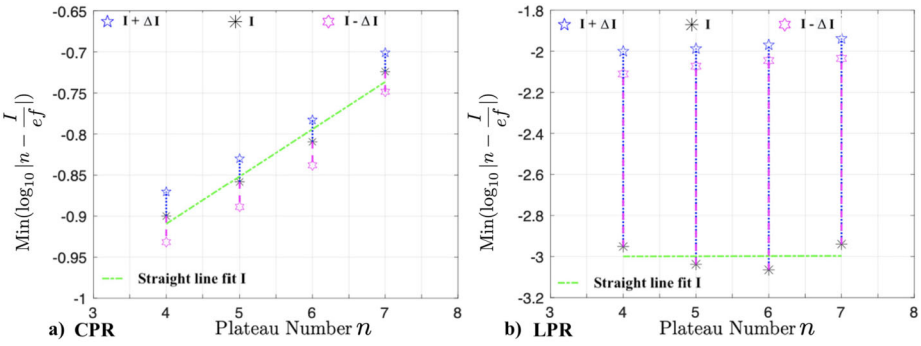


**Figure 4** a) Min($\log_{10}|n - \frac{I}{ef}|$) versus Plateau Number (n) in the CPR. b) Min($\log_{10}|n - \frac{I}{ef}|$) versus Plateau Number (n) in the LPR. In both plots the uncertainty is given by including the uncertainty in the measured current in the Min log calculation. A straight line fit is provided in both cases to show the general trend

Utilising such a pump with a multiple integer number of electrons transported per cycle, offers clear advantages over multiple electron pumps in parallel with single electrons pumped per cycle [29] where the complications in experimental setup and uncertainty from each pump, which adds linearly, is avoided. Such a combination of parallel pumps would not allow a state of multiple entangled electrons rending them inappropriate for more advanced quantum interference measurements.

Figure 4 a) and b) show the minimum values of Min($\log_{10}|n - \frac{I}{ef}|$) for plateaus $n = 4$ to $n = 7$ in both the CPR and LPR respectively. $\Delta I$ is the uncertainty in the reading taken from the SMU and is given by $0.050\%I + 200$ fA. $\Delta I$ is added and then subtracted separately to the current $I$ reading before calculating $\log_{10}|n - \frac{I}{ef}|$ such that two values are determined giving the range in uncertainty for $I$. This is shown in Fig. 4a) and b) where a straight line fit to Min($\log_{10}|n - \frac{I}{ef}|$) is given. In the CPR the accuracy of the pumped current degrades linearly as more electrons are pumped per cycle. In the case of the LPR there appears to be no change in the accuracy in pumped current as the number of electrons pumped through the QD per cycle is increased. In the CPR the demonstration of high pumped accuracy of below $2 \times 10^{-7}$ at a current of around 100 pA has been demonstrated [30] in high fields with work by Hohls et al. [31] uncertainties of the order $10^{-6}$ were shown. These results however were achieved with only a single electron $n = 1$ pumped per cycle, with no work shown on the accuracy achieved for a higher number $n > 1$ of electrons per cycle. The work here was also limited by the capabilities of the measuring setup which is not of the metrological grade as utilised in key meteorological labs around the world.

## 3 Discussion

To explain the experimental findings and account for the unprecedented improvement in robustness and accuracy for a higher integer number of pumped electrons per cycle in the LPR, we present analysis on the key design and operational parameters. Pumps operating in the CPR have until recently [24] been defined with a finger-finger (FF) gate geometry as apposed to a finger-split (FS) geometry [32] as is utilised in this work. We define first the screened potential seen by the 2DEG by the different gate geometries in both regimes. This difference in device design, we claim is fundamental to the key experimental observations made in this paper. We further explore the two-dimensional form of the QD potential and determine where the minima form and the effect the lateral modes (LMs)(see Fig. 7) have

on the dot. The impact of the $V_{SD}$ bias on the defining gate potentials is also studied, paying attention to the minima of the potential as well as the maximum height of the exit gate potential. Finally, we examine the single particle energy levels in both regimes for the gate specific screened potential and consider the impact the use of a non-monochromatic RF trapezoidal signal instead of a simple monochromatic sinusoidal signal has on the capture and ejection of electrons during the pump cycle.

### 3.1 Screened potential

We model the region near the gates for both FF gate and FS gate QDs in the adiabatic limit by solving the Laplacian boundary value problem. For a single gate; either split or finger, of width $2b$, a useful analytic approximation [33] along the channel (($y = 0$) see Fig. 7) of the induced charge $\rho_{\text{ind}}$ on the 2DEG is:

$$\rho_{\text{ind}}(x,0) = \frac{C_G}{d}\frac{e^{\pi x/d}(1-e^{2\pi b/d})}{(e^{\pi b/d}+e^{\pi x/d})(1+e^{\pi (x+b)/d})}, \tag{1}$$

where $d$ is the distance between gates and 2DEG, and $C_G$ has the controlling factor

$$C_G \propto \frac{2V_G}{1+e^{\pi a/d}}, \tag{2}$$

where $2a$ is the width of the gap in a split gate. $a = 0$ corresponds to a finger gate, and $V_G$ is the potential applied to the gate. The proportionality constant may be found from a single numerical evaluation of the potential. The potential on the 2DEG is set to zero, as it is grounded. Assuming a linear response, the screened potential within the 2DEG may be approximated by

$$\phi_{\text{scr}} = -\frac{\pi\hbar^2\epsilon}{m_e q_e^2}\rho_{\text{ind}}, \tag{3}$$

where $\epsilon$ is the permittivity of the substrate, $m_e$ and $q_e$ are the electron mass and charge respectively [33].

### 3.2 Coupling of gate energies and the effect of bias

We make use of equation (3) to model the two-gate potential defining the QD in both geometries. The following discussion only considers the dot potential in one dimension ($y = 0$). The peak in potential energy of the exit barrier along the center of the channel ($U_{\text{ext}}$) is proportional to the voltage applied to the exit gate ($V_{\text{ext}}$). Increasing the size of the gap in the split-gate lowers the coupling between $V_{\text{ext}}$ and $U_{\text{ext}}$ such that the same change in $V_{\text{ext}}$ results in a smaller change in $U_{\text{ext}}$. In Fig. 5a) the profile of screened potential energy along the $y = 0$ channel for a FF gate pump operating in the CPR is shown. In 5b) the profile of screened potential energy along the $y = 0$ channel for a FS gate pump operating in the LPR is shown. The dotted blue and red curves show the form of the harmonic oscillator potential which is used as an approximation to determine the minima and curvature of the QD potential (see Coupling to Lateral Modes section for more detail).

In the CPR, the exit gate finger-gate with zero gap, results in the strong coupling between $V_{\text{ext}}$ and $U_{\text{ext}}$. This is in contrast to the split-gate in the LPR where the much lower

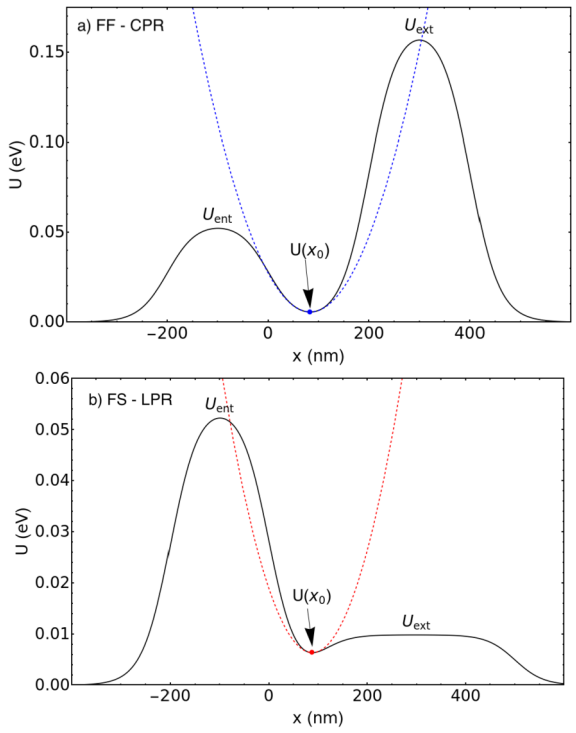


**Figure 5** Profile of screened potential energy along channel $y = 0$ showing the entrance $U_{ent}$ and exit $U_{ext}$ barrier heights for a) FF operating in the CPR and b) FS operating in the LPR. Each is linear in the applied voltages $V_{ent}$ and $U_{ext}$ respectively. Here $V_{ent}$ is −1 V and $V_{ext}$ is −3 V in both plots

coupling between $V_{ext}$ and $U_{ext}$ results in a smaller dot potential. There is clearly an order of magnitude increase for the potential $U_{ext}$ of the finger gate in the CPR versus the potential $U_{ext}$ of the split gate in the LPR despite the same voltages applied($V_{ext} = -3$ V). The entrance finger gate in both regimes has the same applied voltage of $V_{ent} = -1$ V. The minimum in the QD potential energy for fixed gate voltages is indicated in the figures by $U(x_0)$. From the figures not just the magnitude of the minima differ (CPR $U(x_0) \approx 4.5$ meV, LPR $U(x_0) \approx 6.5$ meV) but so to the position in $x$ (CPR $x \approx 80$ nm, LPR $x \approx 90$ nm). This difference will become more apparent when the potential is explored in two dimensions later in the discussion.

We now consider the bias voltage $V_{SD}$ across the pump which has a dramatic effect on the pump maps as observed in the experimental data even when $V_{SD}$ is much smaller than the voltages applied to the gates. The effect of $V_{SD}$ on the electrostatic potentials near the gates is negligible, however we are not interested in the potential on the 2DEG (which must vanish in our model) but instead the screened potential within the 2DEG, which is smaller by around an order of magnitude compared to the applied gate potentials. We model the bias within the 2DEG as a phenomenological addition [34] to the screened potential

$$\phi = \phi_{\text{bias}} + \phi_{\text{scr}}, \tag{4}$$

where along the channel one has

$$\phi_{\text{bias}}(x) = \frac{V_{SD}}{2}\left[1 + \tanh\left(\frac{5x}{2b}\right)\right] \tag{5}$$

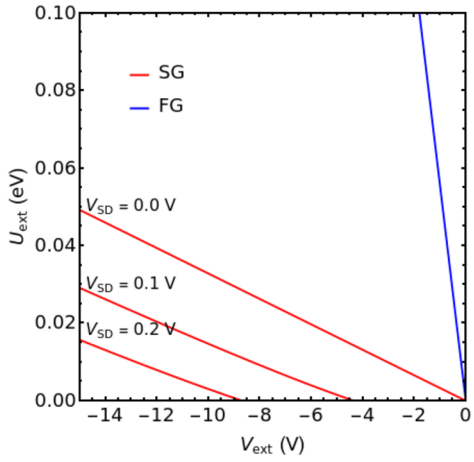


**Figure 6** Different coupling strengths between the voltage applied to the exit gate and the resulting exit barrier height in the CPR and the LPR. The lower coupling in the LPR allows for a fine-tuned probing of the charging states of the quantum dot resulting in longer plateaus in $V_{ext}$. Applying a forward bias in the LPR further lowers the exit barrier

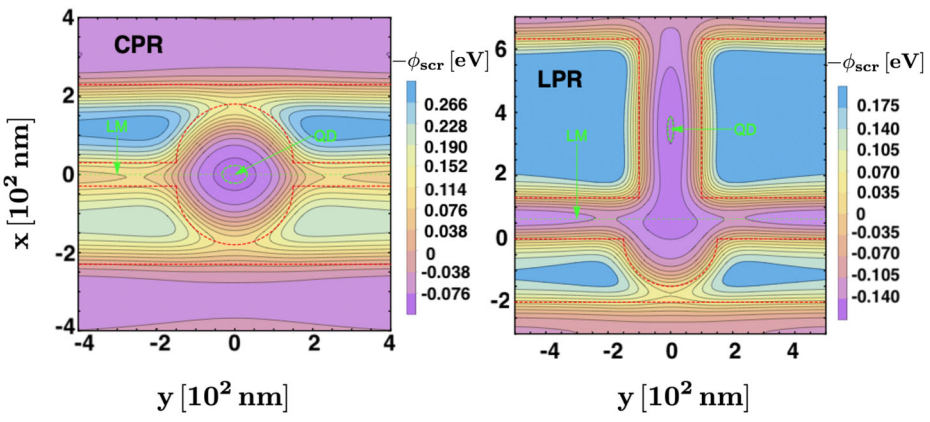


**Figure 7** Screened potential due to FF pump operating in the CPR (left) and FS pump operating in the LPR(right) showing QD position and lateral modes. The doted red lines indicate the outline of the Ti/Au gate structures fabricated using electron beam lithography in the measured devices

For a forward bias, this effectively lowers the barrier height of a split-gate, as shown in the labelled curves in Fig. 6, where the coupling strength of the exit gate voltage $V_{ext}$ to barrier energy height $U_{ext}$ is shown for a split gate (red) with a gap of $a$ = 200 nm in the LPR and finger gate (blue) $a$ = 0 nm in the CPR.

Both gates have a width of 400 nm, so the difference in coupling strength is only dependent on the size of the gap. The lower coupling evident in the split-gate allows for finer control of the exit barrier height that results in higher resolution probing of the energy levels in the quantum dot at ejection. This is a contributing factor to the longer plateaus in $V_{ext}$ visible in the LPR data. The single particle energy levels are explicitly determined later on in this discussion. The change in applied bias $V_{SD}$ is shown only for the split-gate as $V_{SD}$ has been shown experimentally to have little to no effect on the finger-gate and pumping direction [19]. An increase in forward bias shows a decrease in coupling strength in the

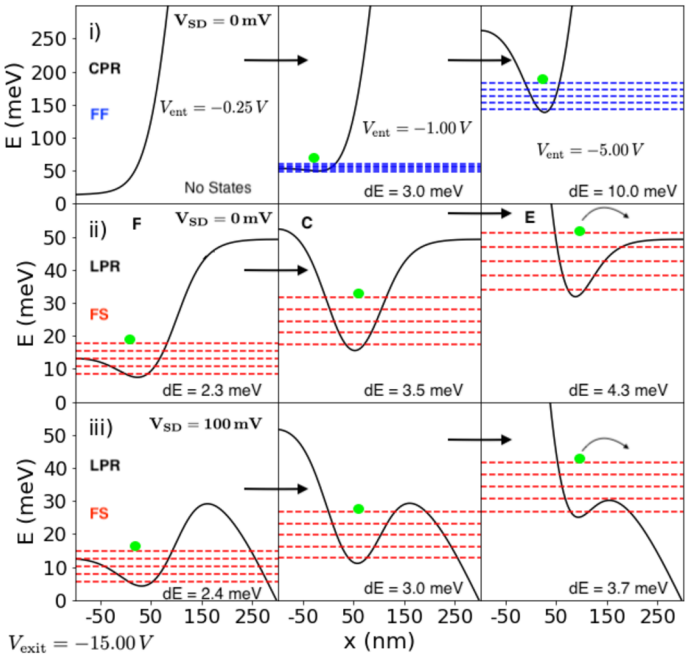


**Figure 8** Center-channel potential (solid line) and energy level spacing (dashed lines) over the course of the pumping cycle at a fixed exit gate voltage. The energy level spacing increases from capture as the curvature of the quantum dot increases. (i) The high exit barrier in the CPR suppresses pumping. (ii) The exit barrier in the LPR with zero bias voltage is low enough to allow a single electron to be pumped. (iii) Applying a forward bias of 100 mV in the LPR lowers the exit barrier allowing multiple electrons to be pumped

split-gate, further increasing the resolution of the exit gate with applied voltage. This too contributes to the enhancement in robustness of pumped electrons and dot size as seen from the pumped electron data in the LPR.

### 3.3 Coupling to lateral modes

For a more representative form of the dot potential and to determine any relevant differences that arise from the different gate geometries in both regimes, the problem is further explored in two-dimensions. A Taylor expansion of the screened potential of the QD at the minima is taken to second order. From this, the curvature in the potential minima in the $x$ and $y$ directions is found. In Fig. 5a) the blue dotted parabola depicts the form of this expanded and approximated potential in the CPR whilst the red dotted parabola in Fig. 5b) depicts the expanded and approximated potential in the LPR. Due to these potentials, the resulting spectrum of single particle states is therefore the sum of two oscillators with 'spring constants' set by $\partial_{xx}\phi$ and $\partial_{yy}\phi$

$$E_{n_x,n_y} = \hbar\omega_x\left(n_x + \frac{1}{2}\right) + \hbar\omega_y\left(n_y + \frac{1}{2}\right) \tag{6}$$

In Fig. 7 the screened 2D potential of the QD for both regimes is shown [33]. For a FF gate pump operating in the CPR, the QD minima (green circle with QD labelled arrow) forms approximately midway between the two finger-gates, where the lateral curvature $\partial_{yy}\phi$ is *small*. For a FS pump operating in the LPR, the QD minima (green circle with QD labelled arrow) forms further along the channel close to the middle of the split-gate, where

the lateral confinement is *large*. Lateral modes (LMs) are also indicated in the figures. In both device geometries (FF and FS) the lateral modes offer a reservoir of sates that can either be occupied and act as a local unwanted source of electrons to the QD or remain empty and act as a local unwanted drain to the QD. The LMs therefore contribute to the level of uncertainty in the pumped current during the pump cycle. The potential energy of the LMs in the FS gate pump operating in the LPR is found to be more positive than the FF gate pump operating in the CPR, but are further from the QD minima. Consequently, the coupling of the LMs to the dot are therefore weaker than in the CPR, where a near-continuum of states couple more readily to the QD.

### 3.4 Single particle energy states

We now investigate the evolution of the single particle states in the QD during the pump cycle for both gate geometries (FF vs FS) and demonstrate how the application of a forward bias can increase the number of pumped electrons through FS gated QDs.

In Fig. 8 strip i) the time evolution (black arrows) of the pump cycle is shown in the CPR where a FF gate geometry is used to define the QD. Here the potential at the center of the channel is modelled as a superposition of the screened potential from two 200 nm wide entrance finger-gates with one situated at $x_{\text{ent}} = -100$ nm, and the other at 100 nm. In Fig. 8 strip ii) and iii) the time evolution (black arrows) of the pump cycle is shown in the LPR where a FS gate geometry is used to define the QDs. The potential at the center of the channel is modelled as a superposition of the screened potential from a 200 nm wide entrance finger-gate situated at $x_{\text{ent}} = -100$ nm, and a 400 nm wide exit split-gate situated at $x_{\text{ext}} = 300$ nm with a gap of 200 nm. In Fig. 8 strip i) and ii) the SD bias is set to 0 mV whilst in strip iii) the SD bias is to 100 mV. Gate voltages are applied to the entrance and exit gates as indicated in the figure, where the $V_{\text{ent}}$ values (as marked in the first row) is the the same for all entrance gates in the corresponding column and the exit gate is set to $V_{\text{ext}} = -15.00$ mV for all plots. The energy level spacing is approximated using the curvature of the resultant screened potential of the surface gates as shown in Fig. 5a) and 5b). The curvature is given by the second order power series expansion centered on the local minimum of the potential ($x_0$), allowing the system to be approximated as a quantum harmonic oscillator with an energy spectrum

$$E_n = \hbar\omega\left(n + \frac{1}{2}\right), \tag{7}$$

where $\omega$ is given by the curvature of the potential at $x_0$.

$$m\omega^2 = \partial_x^2 U(x)|_{x_0} \tag{8}$$

The formation of the quantum dot differs substantially between the regions i),ii) and iii). We label the first column (F) as the start of the formation of the QD, the second column (C) the capture of electrons in the QD and the third column (E), the ejection of the no longer confined electrons. All labelling is taken with respect to the LPR with SD= 0 mV. In all three cases, the curvature of the QD is low at the start of the pump cycle and increases as the entrance barrier rises. This results in a higher energy level spacing at ejection than at capture as is visible from the spacing between the single particle states (dotted lines (blue and red)) in all three regimes. The dense blue dotted lines in the CPR for $V_{\text{ent}} = -1.00$ V

indicate a smaller single particle energy gap when compared to all the other cycles in Fig. 8. The spacing between energy levels $dE$ is indicated in each figure. When the entrance barrier reaches its maximum, all states that are below the exit barrier remain trapped within the dot limiting the pumped current. In the LPR, despite the same voltages applied to both the entrance and exit barriers as in the CPR, states appear above the exit barrier potential resulting in a non-zero quantised current. Applying a forward bias in the LPR lowers the exit barrier, but not to the extent that this has a major effect at capture. Therefore the same number of electrons are captured, but more of the captured electrons are pumped as multiple energy levels are above the potential energy of the exit barrier. This model indicates the mechanism by which increasing the forward bias allows more electrons to be pumped as seen experimentally in Fig. 2. Whilst $V_{\mathrm{SD}}$ does have an effect on the ejection of the electrons from the pump in a similar way to an increase in RF signal amplitude [22], the $V_{\mathrm{SD}}$ also directly impacts the resolution of the exit gate voltage by changing the coupling of the voltage applied to the energy as indicated in Fig. 6. In our model we make no claims regarding the depth of the dot between the CPR and LPR rather we highlight the increase in resolution in the exit gate with split-gate configuration over the finger-gate design used in pumps operating in the CPR. Thermal broadening remains a problem contributing to the uncertainty in pumped current in both regimes.

### 3.5 Non-monochromatic entrance gate RF potentials

The effect on the pump map of changing from a sinusoidal wave to a trapezoidal non-monochromatic wave driving the entrance gate was discussed in the Pumpmaps section earlier on. In an attempt to understand this phenomena we model the gate as a transmission line with distributed inductance (L), capacitance (C), and resistance (R) per unit length. We find that the potential near the channel ($y \approx 0$) (see Fig. 7) develops qualitatively new features when the driving potential is non-harmonic.

In Fig. 9 we plot the effective potential difference between the 2DEG and finger gate at $y = 0$. In Fig. 9a), the harmonic input signal $V_{\mathrm{in}}$ (black line) (that is the output from the signal generator) appears along with the effective RF gate potential ($V_{\mathrm{G1}}$,$V_{\mathrm{G2}}$,$V_{\mathrm{G2}}$), where each $G_i$ with $i = 1, 2, 3$ has slightly different geometric parameters as well as R,L and C.

In addition to the irrelevant horizontal shifts (in the case of $V_{\mathrm{G1}}$ a large shift due to the choice of R,L and C) all modelled effective potentials remain symmetric around zero volts as is the case for the harmonic input signal $V_{\mathrm{in}}$. This is not the case for the trapezoidal input (black line) in Fig. 9b). Here all modelled gates $V_{\mathrm{G1}_i}$ have a similar horizontal shift as for the sinusoidal signal but there is a clear change is the symmetric behaviour around zero volts. This manifests as an asymmetric change in the maximum and minimum in amplitude of the effective RF signal as shown by the red and blue arrows in Fig. 9b). This means that the effective range of AC voltage near the channel can differ from that of the signal from the RF generator. This has a direct impact over the full cycle of pump operation from loading the dot with electrons from the source to ejecting the electrons to the drain over the split gate exit barrier. A full analysis of these effects is the subject of ongoing work. The clear differences seen here in this model between the amplitude of non-monochromatic RF signal and a simple monochromatic sinusoidal signal offers some insight into the origins of the differences observed experimentally.

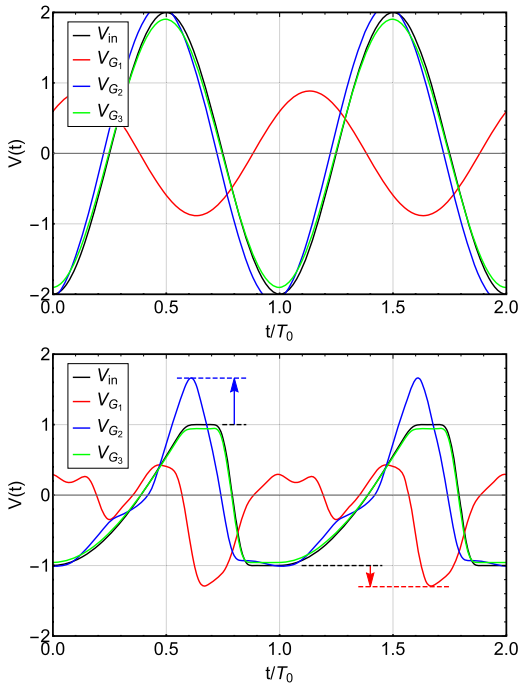


**Figure 9** Comparison of driving potential ($V_{in}$, black lines) and effective potential near centre of finger gate $V_G$. The red, blue, and green lines are $V_G$ for slightly different gate parameters. Top: Sinusoidal input. Bottom: Trapezoidal input

## 4 Conclusion

We have experimentally demonstrated an on demand single electron pump operating in the LPR which delivers multiple ($n > 1$) electrons per cycle in zero magnetic field with a plateau length over two orders of magnitude greater than what is produced in pumps for $n > 1$ operating in the CPR. In the LPR we have shown the pumping accuracy of plateaus for $n > 4$ to remain unchanged as the number of electrons pumped per cycle is increased. For the delivery of $n = 7$ electrons pumped per cycle an accuracy of 164 ppm in the LPR versus 27,221 ppm in the CPR was observed. Such an improvement in the stability and robustness when pumping a high integer number of electrons per cycle offers exciting new opportunities for experimental work in quantum transport measurements. These results were presented in zero magnet field $B = 0$. Despite high magnetic fields being utilised in many electron quantum optics experiments, several low fields ($T < 1$) effects such as electron focusing and skipping orbit experiments [35, 36] as well as phenomena that utilise the Ahronov Bohm effect [37] would be quenched by the large fields used in the field pumps operating in the CPR.

Future work will determine the energies at which these multiple electrons leave the quantum dot. If electrons are found to leave in degenerate states these multi-electron pumps will have a direct application in quantum information and entanglement related experiments, where pump accuracy at the same level as metrological applications such as the standard for electrical current [38] is not required. Furthermore, we have demonstrated the ability to increase the number of electrons pumped per cycle in the LPR without any discernible change in the pumpmap or accuracy of delivered electrons with a simple change in $V_{SD}$ bias. We presented analysis on how this new pumping regime is realised by

investigating the screened potential seen by the 2DEG for different gate geometries (FF, FS) in both regimes. The single electron energy levels in the different pumping regimes were modelled allowing for a clear picture of how these single particle energy levels evolve during the pump cycle and how they differ between the two regimes. The modelling of the two-dimensional potential system of the dynamic quantum dot allowed for study of the lateral modes in the vicinity of the QD, which have a direct impact on the uncertainty in the pumped current, once again highlighting the discrepancies between the two pumping regimes. This work together with the effects of the $V_{SD}$ bias on the defining dot potential as well as the true effective form of the applied RF signal (sinusoidal versus trapezoidal), as seen by the electrons in the 2DEG, has helped to explain some of the fundamental mechanisms responsible for the vastly different electron pumping outcomes in the CPR and LPR.

**Acknowledgements**
This work was supported by the UK Engineering Physical Sciences Research Council, grants EP/K004077/1, EP/R029075/1, EP/P021859/1, the National Research Foundation of South Africa and Sasol Ltd.

**Abbreviations**
QD, Quantum Dot; LPR, Long Pumping Regime; CPR, Conventional Pumping Regime; DAQ, Data Aquistion; SMU, Source Measure Unit; RF, Radio Frequency; $V_{SD}$, Source-Drain Voltage; $V_{ent}$, Entrance Gate; $V_{exit}$, Exit Gate; $\mu_s$, Fermi level Source; $\mu_d$, Fermi level Drain; FF, Finger-finger; FS, Finger-Split; LM, Lateral modes.

**Availability of data and materials**
The datasets used and/or analysed during the current study are available from the corresponding author on reasonable request.

## Declarations

**Ethics approval and consent to participate**
Not applicable.

**Competing interests**
The authors declare no competing interests.

**Author contributions**
M.D.B, H.H and D.G conceived the experiment, setup and ran the measurements, analysed and interpreted the data. H.H. designed and processed the devices. M.D.B produced the experimental data plots and wrote the article. D.M and S.A carried out all the modelling, produced the simulation plots and contributed to the drafting of the paper. T.M carried out the ebeam lithography. H.E.B and D.A.R developed and grew the GaAs/AlGaAs heterostructures used. M.P. provided support, references, and useful discussions. All authors reviewed the manuscript.

**Author details**
[1]Department of Physics, University of Cape Town, Rondebosch, Cape Town, 7700, South Africa. [2]London Centre for Nanotechnology and Dept. of EE, University College London, Kiel, WC1A 0AH, UK. [3]Departmet of Physics, Cambridge University, Cambridge, CB3 0HE, UK.

Received: 19 June 2023 Accepted: 23 October 2023 Published online: 31 October 2023

**References**

1. Bäuerle C, Glattli DC, Meunier T, Portier F, Roche P, Roulleau P, Takada S, Waintal X. Coherent control of single electrons: a review of current progress. Rep Prog Phys. 2018;81(5):056503. https://doi.org/10.1088/1361-6633/aaa98a.
2. Edlbauer H, Wang J, Crozes T, Perrier P, Ouacel S, Geffroy C, Georgiou G, Chatzikyriakou E, Lacerda-Santos A, Waintal X, Glattli DC, Roulleau P, Nath J, Kataoka M, Splettstoesser J, Acciai M, da Silva Figueira MC, Öztas K, Trellakis A, Grange T, Yevtushenko OM, Birner S, Bäuerle C. Semiconductor-based electron flying qubits: review on recent progress accelerated by numerical modelling. EPJ Quantum Technol. 2022;9:21. https://doi.org/10.1140/epjqt/s40507-022-00139-w.
3. Turchette QA, Hood CJ, Lange W, Mabuchi H, Kimble HJ. Measurement of conditional phase shifts for quantum logic. Phys Rev Lett. 1995;75:4710–3. https://doi.org/10.1103/PhysRevLett.75.4710.
4. Dupont-Ferrier E, Roche B, Voisin B, Jehl X, Wacquez R, Vinet M, Sanquer M, De Franceschi S. Coherent coupling of two dopants in a silicon nanowire probed by Landau–Zener–Stückelberg interferometry. Phys Rev Lett. 2013;110:136802. https://doi.org/10.1103/PhysRevLett.110.136802.
5. DiVincenzo D. IBM: the physical implementation of quantum computation. Fortschr Phys. 2000;48:771–83. https://doi.org/10.1002/1521-3978(200009)48:9/113.0.CO;2-E.

6. Yamamoto M, Takada S, Bäuerle C, Watanabe K, Wieck AD, Tarucha S. Electrical control of a solid-state flying qubit. Nat Nanotechnol. 2012;7(4):247–51. https://doi.org/10.1038/nnano.2012.28.
7. Ji Y, Chung Y, Sprinzak D, Heiblum M, Mahalu D, Shtrikman H. An electronic Mach–Zehnder interferometer. Nature. 2003;422(6930):415–8. https://doi.org/10.1038/nature01503.
8. Ubbelohde N, Hohls F, Kashcheyevs V, Wagner T, Fricke L, Kästner B, Pierz K, Schumacher HW, Haug RJ. Partitioning of on-demand electron pairs. Nat Nanotechnol. 2015;10(1):46–9. https://doi.org/10.1038/nnano.2014.275.
9. Gumbs G, Huang D, Blumenthal MD, Wright SJ, Pepper M, Abranyos Y. Spin-split excitation gap and spin entanglement of a pair of interacting electrons in a quantum dot. Semicond Sci Technol. 2009;24:115001. https://doi.org/10.1088/0268-1242/24/11/115001.
10. Fletcher JD, See P, Howe H, Pepper M, Giblin SP, Griffiths JP, Jones GAC, Farrer I, Ritchie DA, Janssen TJBM, Kataoka M. Clock-controlled emission of single-electron rightave packets in a solid-state circuit. Phys Rev Lett. 2013;111:216807. https://doi.org/10.1103/PhysRevLett.111.216807.
11. Ubbelohde N, Freise L, Pavlovska E, Silvestrov PG, Recher P, Kokainis M, Barinovs G, Hohls F, Weimann T, Pierz K, Kashcheyevs V. Two electrons interacting at a mesoscopic beam splitter. Nat Nanotechnol. 2023;18(7):733–40. https://doi.org/10.1038/s41565-023-01370-x.
12. Brange F, Flindt C. Interacting electrons collide at a beam splitter. Nat Nanotechnol. 2023;18(7):696–7. https://doi.org/10.1038/s41565-023-01389-0.
13. Shilton J, Mace D, Talyanskii M, Simmons M, Churchill AC, Ritchie D. Effect of spatial dispersion on acoustoelectric current in a high-mobility two-dimensional electron gas. Phys Rev B. 1995;51:14770–3. https://doi.org/10.1103/PhysRevB.51.14770.
14. Shilton J, Mace D, Talyanskii M, Galperin Y, Simmons M, Pepper M, Ritchie D. LETTER TO THE EDITOR: On the acoustoelectric current in a one-dimensional channel. J Phys Condens Matter. 1995;8:L337. https://doi.org/10.1088/0953-8984/8/24/001.
15. Talyanskii V, Shilton J, Pepper M, Cunningham J, Smith C, Ford C, Linfield E, Ritchie D, Jones G. Single-electron transport in a one-dimensional channel by high-frequency surface acoustic waves. Phys Rev B. 1997;56:15180–4. https://doi.org/10.1103/PhysRevB.56.15180.
16. Delsing P, Likharev KK, Kuzmin LS, Claeson T. Time-correlated single-electron tunneling in one-dimensional arrays of ultrasmall tunnel junctions. Phys Rev Lett. 1989;63:1861–4. https://doi.org/10.1103/PhysRevLett.63.1861.
17. Keller MW, Martinis JM, Zimmerman NM, Steinbach AH. Accuracy of electron counting using a 7-junction electron pump. Appl Phys Lett. 1996;69(12):1804–6. https://doi.org/10.1063/1.117492.
18. Kouwenhoven LP, Johnson AT, van der Vaart NC, Harmans CJPM, Foxon CT. Quantized current in a quantum-dot turnstile using oscillating tunnel barriers. Phys Rev Lett. 1991;67:1626–9. https://doi.org/10.1103/PhysRevLett.67.1626.
19. Blumenthal MD, Kaestner B. Gigahertz quantized charge pumping. Nat Phys. 2007;3:343–7.
20. Wright SJ, Blumenthal MD, Gumbs G, Thorn AL, Pepper M, Janssen TJBM, Holmes SN, Anderson D, Jones GAC, Nicoll CA, Ritchie DA. Enhanced current quantization in high-frequency electron pumps in a perpendicular magnetic field. Phys Rev B. 2008;78:233311. https://doi.org/10.1103/PhysRevB.78.233311.
21. Kaestner B, Kashcheyevs V, Hein G, Pierz K, Siegner U, Schumacher HW. Robust single-parameter quantized charge pumping. Appl Phys Lett. 2008;92(19):192106. https://doi.org/10.1063/1.2928231.
22. Kaestner B, Kashcheyevs V, Hein G, Pierz K, Siegner U, Schumacher H. Robust single-parameter quantized charge pumping. Appl Phys Lett. 2008;92(19):192106.
23. Giblin SP, Kataoka M, Fletcher JD, See P, Janssen TJBM, Griffiths JP, Jones GAC, Farrer I, Ritchie DA. Towards a quantum representation of the ampere using single electron pumps. Nat Commun. 2012;3:930. https://doi.org/10.1038/ncomms1935.
24. Howe H, Blumenthal M, Beere HE, Mitchell T, Ritchie DA, Pepper M. Single-electron pump with highly controllable plateaus. Appl Phys Lett. 2021;119(15):153102. https://doi.org/10.1063/5.0067428.
25. Janssen TJBM, Hartland A. Accurate measurement of currents generated by single electrons transported in a one-dimensional channel. IEE Proc Sci Meas Technol. 2000;147(4):174–6. https://doi.org/10.1049/ip-smt:20000449.
26. Wright SJ, Thorn AL, Blumenthal MD, Giblin SP, Pepper M, Janssen TJBM, Kataoka M, Fletcher JD, Jones GAC, Nicoll CA, Gumbs G, Ritchie DA. Single- and few-electron dynamic quantum dots in a perpendicular magnetic field. J Appl Phys. 2011;109:102422. https://doi.org/10.1063/1.3578685.
27. Bernd K, Vyacheslavs K. Non-adiabatic quantized charge pumping with tunable-barrier quantum dots: a review of current progress. Rep Prog Phys. 2015;78(10):103901. https://doi.org/10.1088/0034-4885/78/10/103901.
28. Giblin SP, Fujiwara A, Yamahata G, Bae M-H, Kim N, Rossi A, Möttönen M, Kataoka M. Evidence for universality of tunable-barrier electron pumps. Metrologia. 2019;56(4):044004. https://doi.org/10.1088/1681-7575/ab29a5.
29. Wright S, Blumenthal M, Pepper M, Anderson D, Jones G, Nicoll C, Ritchie D. Parallel quantized charge pumping. Phys Rev B. 2009;80(11):113303.
30. Stein F, Scherer H, Gerster T, Behr R, Götz M, Pesel E, Leicht C, Ubbelohde N, Weimann T, Pierz K, Schumacher HW, Hohls F. Robustness of single-electron pumps at sub-ppm current accuracy level. Metrologia. 2016;54(1):1. https://doi.org/10.1088/1681-7575/54/1/S1.
31. Hohls F, Kashcheyevs V, Stein F, Wenz T, Kaestner B, Schumacher HW. Controlling the error mechanism in a tunable-barrier nonadiabatic charge pump by dynamic gate compensation. Phys Rev B. 2022;105:205425. https://doi.org/10.1103/PhysRevB.105.205425.
32. Kaestner B, Kashcheyevs V, Amakawa S, Blumenthal M, Li L, Janssen T, Hein G, Pierz K, Weimann T, Siegner U et al. Single-parameter nonadiabatic quantized charge pumping. Phys Rev B. 2008;77(15):153301.
33. Davies JH, Larkin IA, Sukhorukov EV. Modeling the patterned two-dimensional electron gas: electrostatics. J Appl Phys. 1995;77(9):4504–12. https://doi.org/10.1063/1.359446.
34. Gloos K, Utko P, Aagesen M, Sørensen CB, Hansen JB, Lindelof PE. Current-voltage characteristics of quantum-point contacts in the closed-channel regime: transforming the bias voltage into an energy scale. Phys Rev B. 2006;73:125326. https://doi.org/10.1103/PhysRevB.73.125326.
35. Molenkamp LW, Staring AAM, Beenakker CWJ, Eppenga R, Timmering CE, Williamson JG, Harmans CJPM, Foxon CT. Electron-beam collimation with a quantum point contact. Phys Rev B. 1990;41:1274–7. https://doi.org/10.1103/PhysRevB.41.1274.

36. Spector J, Stormer HL, Baldwin KW, Pfeiffer LN, West KW. Control of ballistic electrons in macroscopic two-dimensional electron systems. Appl Phys Lett. 1990;56(10):967–9. https://doi.org/10.1063/1.102594. https://pubs.aip.org/aip/apl/article-pdf/56/10/967/7774412/967_1_online.pdf.
37. Webb RA, Washburn S, Umbach CP, Laibowitz RB. Observation of $\frac{h}{e}$ Aharonov–Bohm oscillations in normal-metal rings. Phys Rev Lett. 1985;54:2696–9. https://doi.org/10.1103/PhysRevLett.54.2696.
38. Scherer H, Schumacher HW. Single-electron pumps and quantum current metrology in the revised si. Ann Phys. 2019;531(5):1800371. https://doi.org/10.1002/andp.201800371.

## Publisher's Note